On-line adaptive asynchronous parameter identification of lumped electrical characteristic model for vehicle lithium-ion battery considering multi-time scale effects.

SHI, H., WANG, S., WANG, L., XU, W., FERNANDEZ, C., DABLU, B.E. and ZHANG, Y.

2022

On-line adaptive asynchronous parameter identification of lumped electrical characteristic model for vehicle lithium-ion battery considering multi-time scale effects

Haotian Shi[a], Shunli Wang[a*], Liping Wang[a,b], Wenhua Xu[a], Carlos Fernandez[c], Bobobee Etse Dablu[a], Yongchao Zhang[d]

[a]*School of Information Engineering, Southwest University of Science and Technology, Mianyang 621010, China;*

[b]*State Key Laboratory of Tribology and Institute of Manufacturing Engineering, Department of Mechanical Engineering, Tsinghua University, Beijing 100084, China;*

[c]*School of Pharmacy and Life Sciences, Robert Gordon University, Aberdeen AB10-7GJ, UK;*

[d]*Urumqi Electric Power Supply Company, State Grid Xinjiang Electric Power Co., Ltd., Urumqi 830011, China.*

Abstract: The accurate modeling of lithium-ion batteries is extremely important to improve the reliability of battery management systems, and solving the problem of multi-time scales is extremely beneficial for high-accuracy battery modeling and adaptive asynchronous parameter identification. This paper distinguishes the fast and slow change characteristics of the model resistor-capacitor link parameters, a strong applicability model for the aggregate electrical characteristics of vehicle-mounted lithium-ion batteries based on multi-time scales is established. By combining the advantages of different identification algorithms, an adaptive asynchronous parameter identification strategy is proposed, which solves the problem of data saturation caused by the time scale identification strategy. Then, the complex charge-discharge pulse and the mixed discharge pulse tests are designed explicitly, and the parameter results and terminal voltage tracking effects under different identification strategies are compared. Moreover, the consistency results of the parameter identification test under single-time scale forgetting factor recursive least squares and multi-time scale adaptive asynchronous parameter identification strategy are analyzed. The results show that under different working conditions, the identification

precision of the terminal voltage based on the adaptive asynchronous parameter identification strategy is increased by 0.420% and 1.114% respectively, and the maximum error of parameter consistency is reduced by 158.300%.

Key words: lumped electrical characteristic model; multi-time scales effect; adaptive estimation; system on-line identification; consistency verification analysis

***Corresponding author:** *Shunli Wang. Tel/fax: +86-15884655563. E-mail address: wangshunli@swust.edu.cn.*

1 Introduction

As a key area of strategic emerging industries in various countries, the research and development of the electric vehicle industry have attracted much attention all over the world. Electric vehicles have the incomparable advantages of traditional fuel vehicles and can improve the problems of energy shortage and environmental pollution. The power battery pack is the heart of new energy electric vehicles, and the design of its management system has a great impact on the performance and safety of the vehicle. In the actual operation of the battery management system, the physical quantities that can be directly observed are limited to parameters such as voltage, current, operating time, and temperature, but the information that the driver cares about is often more than that. Therefore, estimating the internal state of the power battery and presenting it to the driver is one of the key tasks in the research and development of new energy vehicles, including the health of the battery, the state of charge, and the charging and discharging characteristics [1]. The battery internal state estimation relies on the high-accuracy of the battery model and high-precision battery internal parameters. At present, most model-based parameter identification algorithms cannot achieve adaptive adjustments to driving conditions [2-3]. Therefore, finding an adaptive parameter identification strategy and a high accuracy battery model will greatly promote the development of the new energy vehicle industry.

For power lithium-ion batteries, battery modeling methods are often different in achieving key aspects such as precision. As domestic and foreign researchers continue to study the construction of equivalent circuit models of lithium-ion batteries, there are many types of lithium-ion battery models. From the simplest and basic internal resistance model to the slightly more complex Thevenin model and partnership for a new generation of vehicles (PNGV) model, the accurate characterization of the internal polarization characteristics of the battery is achieved [4-9]. The dynamic characteristics of the battery pack are simulated to a certain extent. At the same time, to more accurately reflect the changing law of the battery, researchers have developed a variety of resistance-capacitance (RC) equivalent circuit models [10-14]. In addition, compared with the Thevenin model, the PNGV model takes into account the cumulative effect of load current on the lithium-ion battery pack, making it more accurate [15, 16]. In addition, based on the above-mentioned existing traditional equivalent circuit empirical models, researchers have further proposed many more comprehensive modeling methods. Zhang et al. [17] completed the cycle life prediction based on the hybrid model of batteries. Fenner et al. [18] constructed a comprehensive model test for variable load battery simulation. Cecilio et al. [19] improved the energy and power capacity of the battery pack by studying the construction method of the equivalent circuit model. Bruch et al. [20] established a new parameterization method of reliable equivalent circuit model. Feng et al. [21] studied the method of online testing of internal resistance and solved the problem of online detection of internal resistance from the perspective of parameter estimation. Fridholm et al. [22] studied the recursive estimation method of impedance to improve the precision of the algorithm. Barai et al. [23] studied the time scale effect of internal resistance through the characterization method of lithium-ion batteries. Xu et al. [24] completed the internal state estimation of the physics-based lithium-sulfur battery model. Ragone et al. [25] completed a data-driven estimation of Vehicle batteries charging state based on a multi-physical model. Mesbahi et al. [26] studied the construction method of the lithium-

ion battery kinetics model. In addition to the above-mentioned experience-based ECMs modeling, some scholars also start from the electrochemical reaction mechanism and realize the internal state characterization, analysis, and design of the battery based on the porous electrode theory [27-29]. Mechanism modeling has high accuracy in describing the voltage characteristics of the battery. However, in the mechanism modeling, there are many parameters, the parameter values are difficult to obtain accurately, and the model is too complicated to solve the difficult problems, which makes the online application of the model very difficult. Therefore, from the perspective of practical applications, the equivalent circuit modeling method of lithium-ion batteries occupies an absolute advantage.

Judging from the existing empirical modeling methods, optimization equivalent circuit models (ECMs) have been used extensively in the new energy modeling community, focusing either on the relationship between current excitation and voltage response [30-32]. However, in these long-term battery models, the hysteresis effect inherent in the open-circuit voltage of the battery is often ignored. In addition, from the perspective of battery loading applications, existing studies often simply use the equivalent resistance-capacitance link to characterize the polarization response inside the battery and do not fully consider the multi-time scale of model characteristics. This makes the inconsistency of internal parameters of the battery stand out during the long-term use of the battery. It further has an adverse effect on the estimation of the internal state of the battery and aggravates the discomfort of new energy car users. Given the necessity and urgent needs of lithium-ion battery equivalent modeling, considering the physical meaning of battery internal parameters, it is particularly important to establish a targeted high-fidelity battery model and optimize online parameter identification strategies. Dai et al. [33] first proposed the concept of multi-time-scale online parameter identification, using the traditional second-order RC circuit to expand the research, and tested the accuracy of the multi-time-scale online parameter identification algorithm under cyclic conditions. Among them, the smallest root-mean-square error is

2.1%. However, the author ignored the inherent hysteresis effect of the open-circuit voltage of the battery when modeling the battery cell. Since the open-circuit voltage curves of different batteries have different degrees of the plateau, simple RC circuit modeling will reduce the adaptive adjustment ability of the multi-time scale online parameter identification algorithm to operating conditions when applied. This phenomenon is particularly obvious in Lithium-iron phosphate battery.

In addition to the above-mentioned related research by scholars, other experts in the field have conducted systematic research on battery modeling and parameter identification, and have achieved good results. Wang et al. [34] designed a model-based continuous micro-current charging method for DC micro grid, which improved the charging efficiency of vehicle batteries. Hashemi et al. [35] greatly improved the safety of hybrid aircraft through online estimation design of battery model parameters and health status. Wang et al. [36] established a time-space model of the internal state distribution of lithium-ion batteries, which improved the estimation speed of battery state analysis. Wijewardana et al. [37] realized the dynamic equivalent modeling and state of charge (SOC) estimation of the battery, and improved the precision of battery parameter estimation to a certain extent. Jin et al. [38] studied thermal runaway characteristics of lithium-ion batteries induced by external heating through models and experiments, which provided a basis for improving the safety of batteries. Yang et al. [39] realized SOC adaptive state estimation based on the battery model, which reduced the oscillation in the estimation and improved the estimation precision. Bruen et al. [40] studied equivalent battery modeling and experimental evaluation methods, which eliminated the imbalance of energy and power capacity of the battery pack. In contrast to experimental studies simply identifying the battery model parameters to achieve terminal voltage tracking, there exists, to the best of our knowledge, few studies have been oriented from system's multi-time scales, whereas lack of whole internal chemical reaction perspective may lead to the inconsistency of model parameters.

Based on the above discussion, this paper models the inherent hysteresis characteristics of the open-circuit voltage and couples it with the model-based state-space equation. By clarifying the response mechanism of ions during battery charging and discharging, and considering the multi-time scale effects inside the battery, a lumped electrical characteristic model (LECM) of vehicle-mounted lithium-ion batteries with strong applicability based on multiple time-scales is established. Secondly, to distinguish the gradual fast， and slow change characteristics of the parameters of the RC link of the model, an adaptive asynchronous parameter identification strategy (AAPIS) is designed and implemented, so that the parameter identification can be adaptive to any working conditions. Finally, the verification of the LECM and AAPIS is completed under the complex charge-discharge pulse test (CCDPT) and the mixed discharge pulse test (MDPT), and the physical meaning analysis of the results of parameter identification under different experiments are given. In addition, the terminal voltage tracking effect and parameter identification results based on the multi-time scale AAPIS are compared with the experimental results of the traditional single-time scale forgetting factor recursive least squares (FFRLS).

2 Model framework

2.1 Lumped electrical characteristic modeling

In the process of charging and discharging lithium-ion batteries, the speed of chemical reactions such as the transfer of internal charges, the double-layer effect, and the diffusion of ions in solid particles are quite different, which corresponds to the multi-time scale effect of the battery. The effect of multi-time scales often brings about the problem of cumulative error, which is directly manifested by the inaccuracy of the equivalent circuit model. Since the working condition of pure electric vehicles is most of the time-continuous discharge, the multi-time scale effect is particularly obvious in a pure electric vehicle battery management system (BMS).

To eliminate the impact of the multi-time scale effect on the accuracy of the vehicle-mounted lithium-ion battery model, this paper distinguishes the different external battery characteristics of the battery in the transient state and the steady state. Combined with the hysteresis characteristics of the battery open-circuit voltage (OCV), a highly applicable vehicle-mounted lithium-ion battery lumped electrical characteristics model (LECM) based on the multi-time scale effect is established. The coupling relationship between the models is shown in Fig. 1.

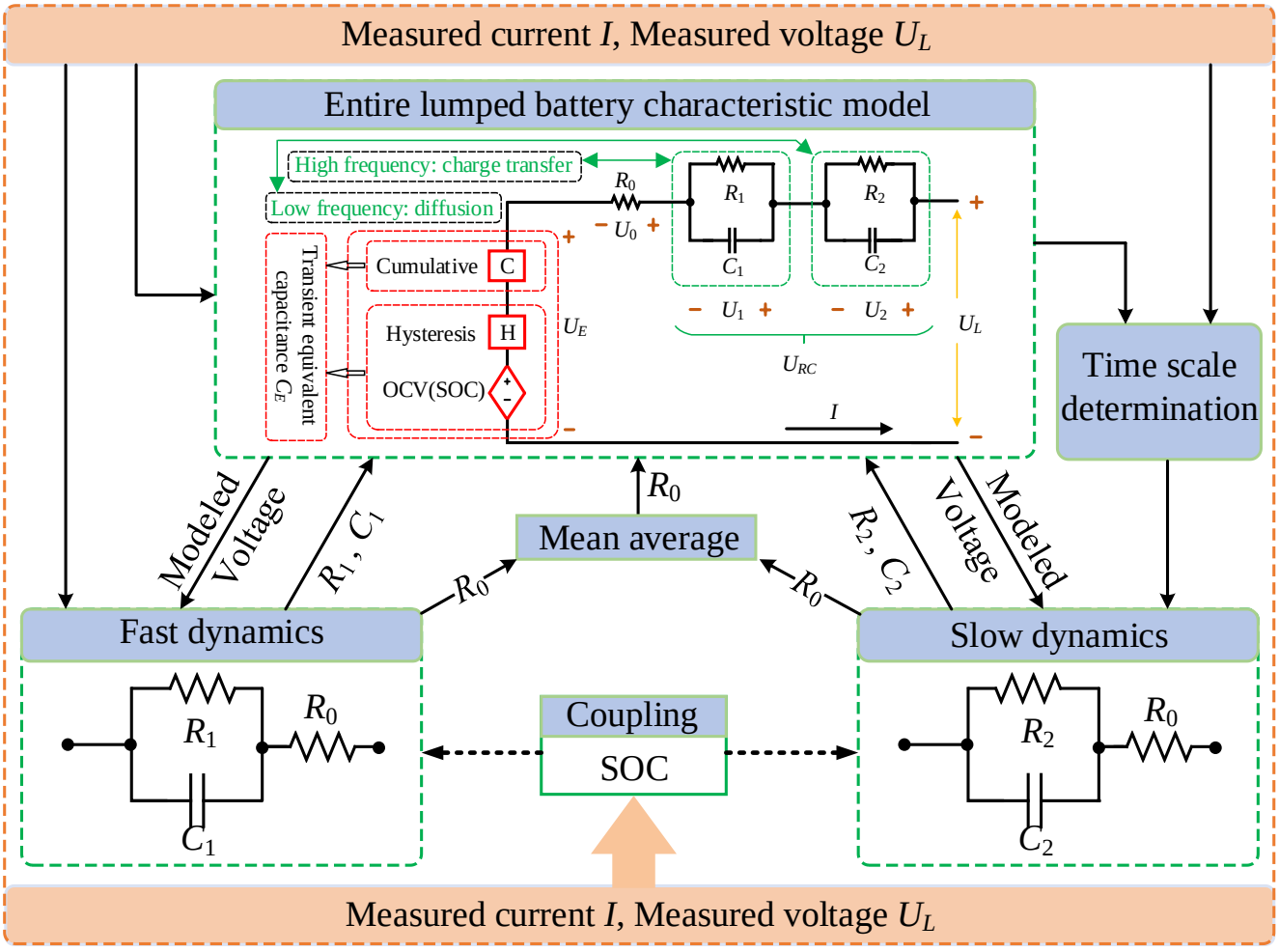

Fig.1 Lumped electrical characteristics model structure

As shown in Fig. 1, the LECM of on-board lithium-ion batteries based on multiple time scales and time-varying effects consists of the OCV part and impedance part. A large number of OCV-SOC calibration experiments show that the open-circuit voltage contains hysteresis characteristics, which is

represented by the H module, and the voltage at both ends of the H module is represented by U_h. Module C is used to characterize the change in open-circuit voltage due to current accumulation. The impedance part is composed of ohmic impedance, electrochemical polarization impedance, and concentration polarization impedance. The ohmic impedance is mainly expressed as the impedance formed by the migration of ions in the electrolyte, expressed by R_0, and its volt-ampere characteristic relationship is expressed as a transient. The two resistor-capacitor (RC) links are used to describe the internal electrochemical polarization and concentration polarization process of the battery during charging and discharging. They are represented by R_1C_1 and R_2C_2 respectively, and the relationship of the volt-ampere characteristics is shown as a gradual change. In addition, module C is used to characterize the change of open-circuit voltage due to current accumulation. C_E is used to equate the transient capacitance of open-circuit voltage at high frequency, and U_E is the voltage across C_E. It can be observed that, when the sampling time is small enough, the open-circuit voltage of the battery is approximately a capacitor. Using this feature, the discretization of the state equation and the online parameter identification of the model can be completed.

2.2 Model-based modular state representation

The accurate OCV-SOC characterization equation needs to consider the hysteresis characteristics of the battery and OCV. By integrating and optimizing the general empirical equation of the electrical characteristic model, combined with the averaging method of multiple experiments, the OCV characterization equation based on the lumped electrical characteristic model of the vehicle-mounted lithium-ion battery with strong applicability is obtained, as shown in Equation (1).

$$U_{OC}(SOC_k) = f(SOC_k) = m_1 + m_2 \ln(SOC_k) + m_3 \ln[1-(SOC_k)] \quad (1)$$

In Equation (1), SOC_k represents the SOC value at time k, m_1-m_3 are the coefficients of the equation,

and the value is determined by the experimental data combined with the recursive least square (RLS) method.

It is worth noting that the value of the hysteresis voltage function generated by the battery during the charge-discharge conversion period is not a simple linear relationship. The force component brought by the historical hysteresis voltage value is combined with the current free component hysteresis voltage value to complete the characterization of the hysteresis voltage in the LECM. Through the current value collected by the BMS, a step function is used to determine the current state of charge and discharge of the system, and then the calculation of the hysteresis voltage is completed, as shown in Equation (2).

$$\begin{cases} U_{h,k+1} = \underbrace{\exp[-\left|\eta I_k \varepsilon \Delta t / Q_N\right|]}_{A_{h,k}} U_{h,k} + \underbrace{[1-\exp(-\left|\eta I_k \varepsilon \Delta t / Q_N\right|)]}_{1-A_{h,k}} \operatorname{sgn}(I_k) M(SOC_k) \\ M(SOC_k) = [U_{OC,chg}(SOC_k) - U_{OC,dchg}(SOC_k)]/2 \end{cases} \tag{2}$$

In Equation (2), $U_{h,k}$ represents the hysteresis voltage value at time k. Q_N represents the rated battery capacity, η is the Coulomb efficiency, ε is the hysteresis decay rate adjustment factor, $U_{OC,chg}$ and $U_{OC,dchg}$ respectively represent the open-circuit voltage during the charging and discharging phases. $M(SOC_k)$ is calculated by charging and discharging OCV. Δt represents the sampling step, and I_k represents the current of the system at time k.

In addition to the OCV-SOC function and hysteresis voltage, the time-domain expression of LECM also includes the discrete form of the RC part. According to the zero input response and zero state response equations in the circuit, the full response equation of the discrete form of the double RC loop in the model can be obtained, as shown in Equation (3).

$$\underbrace{\begin{bmatrix} U_{1,k+1} \\ U_{2,k+1} \end{bmatrix}}_{U_{RC,k+1}} = \underbrace{\begin{bmatrix} \exp(\frac{-\Delta t}{R_1 C_1}) & 0 \\ 0 & \exp(\frac{-\Delta t}{R_2 C_2}) \end{bmatrix}}_{A_{RC}} \underbrace{\begin{bmatrix} U_{1,k} \\ U_{2,k} \end{bmatrix}}_{U_{RC,k}} + \underbrace{\begin{bmatrix} R_1[1-\exp(\frac{-\Delta t}{R_1 C_1})] \\ R_2[1-\exp(\frac{-\Delta t}{R_2 C_2})] \end{bmatrix}}_{B_{RC}} I_k \tag{3}$$

In Equation (3), $U_{1,k}$, and $U_{2,k}$ respectively represent the voltage values across R_1C_1 and R_2C_2 at

time *k*. $U_{RC,k+1,}$ and $U_{RC,k}$ represent the total diffusion voltage across the resistor-capacitor pair at the *k+1* and kth sampling moments respectively. A_{RC} is a zero-input response coefficient matrix, and B_{RC} is a zero-state response coefficient matrix.

The internal reaction mechanism of the battery is complicated, and the various parameters are often accompanied by high-latitude coupling. Based on the representation method of each link of the above model in the time domain state, the state-space equation description suitable for the lumped electrical characteristic model is given, as shown in Equation (4).

$$\begin{bmatrix} SOC_{k+1} \\ U_{RC,k+1} \\ U_{h,k+1} \end{bmatrix} = \begin{bmatrix} 1 & 0 & 0 \\ 0 & A_{RC} & 0 \\ 0 & 0 & A_{h,k} \end{bmatrix} \begin{bmatrix} SOC_k \\ U_{RC,k} \\ U_{h,k} \end{bmatrix} + \begin{bmatrix} -\eta \Delta t / Q_N & 0 \\ B_{RC} & 0 \\ 0 & 1 - A_{h,k} \end{bmatrix} \begin{bmatrix} I_k \\ \mathrm{sgn}(I_k) M(SOC_k) \end{bmatrix} \tag{4}$$

2.3 Discrete representation of state-space equations

The realization of online parameter identification based on LECM requires an exogenous autoregressive model. Using the state-space equation shown in Equation (4), the continuous expression of the terminal voltage of the lumped electrical characteristic model is obtained, as shown in Equation (5).

$$U_L(t) = U_E(t) - U_0(t) - U_{RC}(t) \Leftarrow U_{RC}(t) = U_1(t) + U_2(t) \tag{5}$$

In Equation (5), *t* is a continuous-time variable. It should be noted that when the sampling time is small enough, the open-circuit voltage of the battery is approximately a capacitor, and the voltage across the battery is U_E.

The pull transform is used to make a one-step transformation to Equation (5), and obtain the model terminal voltage output equation in the frequency domain state. Then the transfer function of the lumped electrical characteristic model is obtained, as shown in Equation (6).

$$G(s) = \frac{U_L(s)}{I(s)} = -R_0 - \frac{1}{C_E s} - \frac{R_1}{1 + R_1 C_1 s} - \frac{R_2}{1 + R_2 C_2 s} \tag{6}$$

In Equation (6), C_E is the approximate characterization of the open-circuit voltage of the battery, and s is the Laplace operator. The output equation of the model terminal voltage in the frequency domain is still in continuous form. Therefore, Equation (6) needs to be further transformed to obtain the discrete terminal voltage transfer function in the Z domain, as shown in Equation (7).

$$G(z)=(1-z^{-1})Z\left[\frac{1}{s}G(s)\right]\Rightarrow G(z)=-R_0-\frac{\Delta t\times z^{-1}/C_E}{1-z^{-1}}-R_1+\frac{R_1(1-z^{-1})}{1-az^{-1}}-R_2+\frac{R_2(1-z^{-1})}{1-bz^{-1}} \quad (7)$$

In Equation (7), a and b are calculated as shown in Equation (8).

$$a=\exp(\frac{-\Delta t}{R_1C_1}),b=\exp(\frac{-\Delta t}{R_2C_2}) \quad (8)$$

Combining Equation (6) and Equation (7), the discrete terminal voltage transfer function in the Z-domain is further simplified, and its form is shown in Equation (9).

$$\begin{aligned}G(z)=\frac{\begin{array}{c}\{-R_0+[R_0(a+b+1)+R_1(a-1)+R_2(b-1)-\Delta t/C_E]z^{-1}\\+[-R_0(ab+a+b)+R_1(1+b)(1-a)+R_2(1+a)(1-b)+\Delta t/C_E\,(a+b)]z^{-2}\\+[abR_0+R_1b(a-1)+R_2a(b-1)-\Delta t/C_E\,ab]z^{-3}\}\end{array}}{[1-(a+b+1)z^{-1}+(ab+a+b))z^{-2}-abz^{-3}]}\end{aligned} \quad (9)$$

The discrete transfer function in the Z domain is discrete in the complex frequency domain, and the BMS can only be embedded in the discrete equation in the time domain. Therefore, combining $U(z)=G(z)I(z)$ and Equation (8), the differential equation of the model terminal voltage in the time domain state can be obtained, as shown in Equation (10).

$$U(k)=\alpha_0U(k-1)+\alpha_1U(k-2)+\alpha_2U(k-3)+\beta_0I(k)+\beta_1I(k-1)+\beta_2I(k-2)+\beta_3I(k-3) \quad (10)$$

In Equation (10), U is the terminal voltage U_L of the system. α_0、α_1、α_2、β_0、β_1、β_2 and β_2 are parameters to be identified. Among them, α_0、α_1 and α_2 are related to system output, β_0、β_1、β_2 and β_2 are related to system input. The expansion of each parameter is shown in Equation (11).

$$\begin{cases} \alpha_0 = a+b+1, \alpha_1 = -(ab+a+b), \alpha_2 = ab, \beta_0 = -R_0 \\ \beta_1 = R_0(a+b+1)R_1(a-1) + R_2(b-1) - \Delta t/C_E \\ \beta_2 = -R_0(ab+a+b) + R_1(1+b)(1-a) + R_2(1+a)(1-b) + \Delta t/C_E\ (a+b) \\ \beta_3 = abR_0 + R_1 b(a-1) + R_2 a(b-1) - \Delta t/C_E\ ab \end{cases} \tag{11}$$

The parameter values of R_0, R_1 and R_2 in the model can be obtained through the calculation of Equation (10). Combining Equation (7) with Equation (10) further, the values of C_1 and C_2 can be obtained, and then all the parameters in LEM can be completed. Equation (10) can be rewritten in the form of an exogenous autoregressive model, as shown in Equation (12).

$$\boldsymbol{Y}_k = \boldsymbol{\varphi}_k{}^T \boldsymbol{\theta} \Leftarrow \begin{cases} \boldsymbol{\theta} = [\alpha_0, \alpha_1, \alpha_2, \beta_0, \beta_1, \beta_2, \beta_3] \\ \boldsymbol{\varphi}_k = [U_{k-1}, U_{k-2}, U_{k-3}, I_k, I_{k-1}, I_{k-2}, I_{k-3}] \end{cases} \tag{12}$$

In Equation (12), φ represents the input and output of the system. θ represents the parameter vector of the system to be identified and Y_k represents the terminal voltage output value of the system at time k. Using the online parameter identification algorithm under multiple time scale combined with the historical terminal voltage output value and the current input value of the system, the parameter vector to be identified at each moment of the system is obtained. The values of a and b are solved according to the parameter vector to be identified and completed through the identification of all parameters in the LECM.

2.4 Adaptive asynchronous parameter identification strategy

2.4.1 Multi-time scale identification framework

The voltage response of the battery under the action of current includes both a fast response link and a slow change link, that is, the dynamic characteristics of the battery are distributed in a wide frequency range. The above problems greatly affect the precision of parameter identification, and may even cause the results to oscillate or diverge. At the same time, as the complexity of the model structure increases, the identification of all parameters at the same time scale will increase the amount of

calculation and aggravate the generation of ill-conditioned matrices. To solve the problems caused by multiple battery time scales, this paper proposes an adaptive asynchronous parameter identification strategy. The specific implementation is shown in Fig. 2.

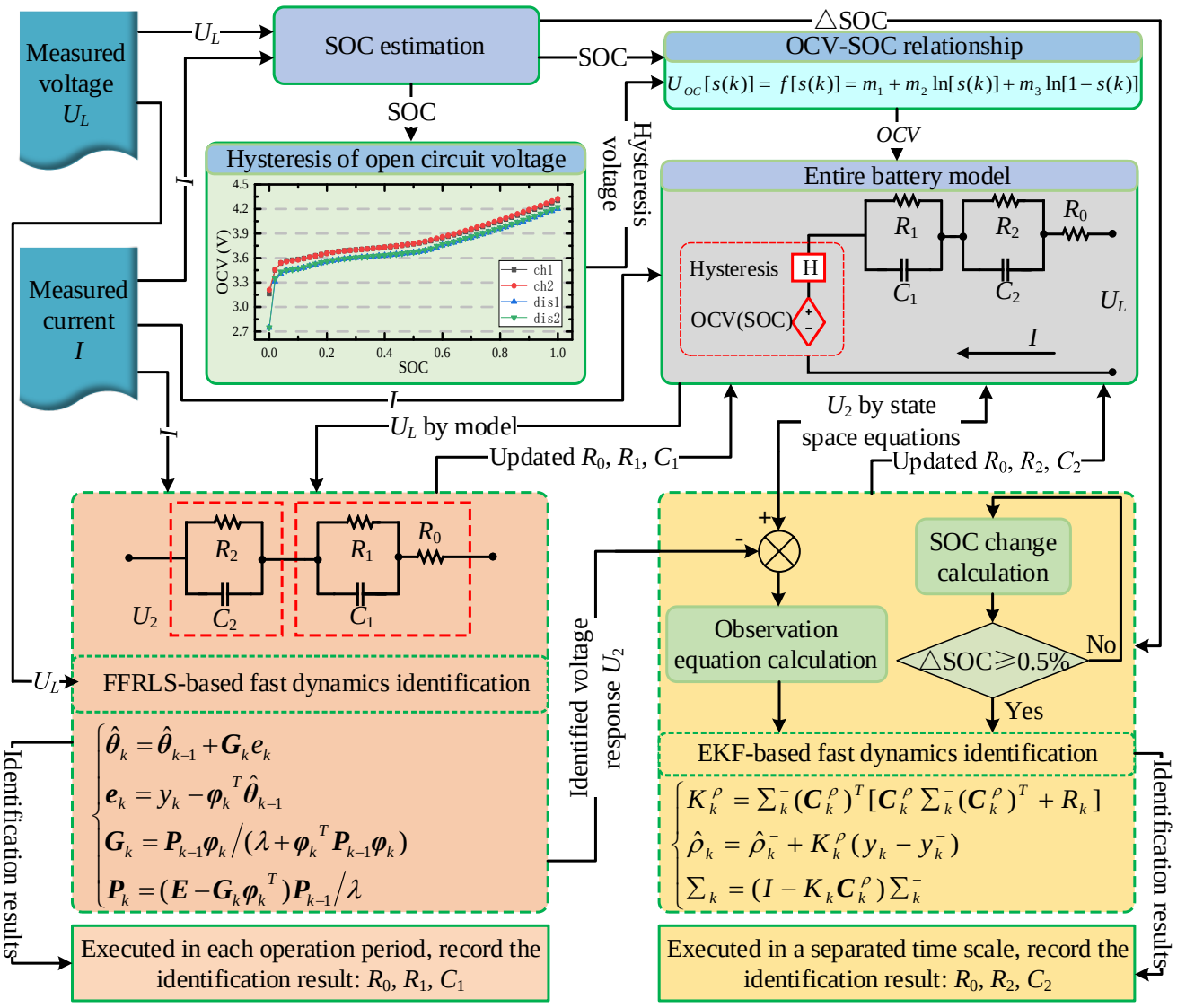

Fig. 2 Adaptive multi-time scale online parameter identification framework

As shown in Fig. 2, first the multi-time scale effect inside the battery is considered, and the model parameter identification at high frequencies based on the FFRLS algorithm is completed. Combining the influence of the battery time-varying effect and the hysteresis effect, the core formula of the FFRLS algorithm is given, as shown in Equation (13).

$$\hat{\boldsymbol{\theta}}_k = \hat{\boldsymbol{\theta}}_{k-1} + \varepsilon_k \tag{13}$$

In Equation (13), ε_k is the correction term of the parameter to be identified in the model at time k. $\hat{\boldsymbol{\theta}}_k$ represents the iterative value of the parameter matrix to be identified at time k. Compared with the traditional recursive least squares (RLS) algorithm, the FFRLS algorithm can enhance the estimation effect of the parameters to be identified. The calculation of the full sequence iterative recursive matrix based on the FFRLS algorithm is as follows.

Step 1: Initialize the parameter matrix to be identified $\hat{\boldsymbol{\theta}}_0$ and the error covariance matrix $\boldsymbol{P}_0$.

$$\hat{\boldsymbol{\theta}}_0 = E[\theta_0], P_0 = E[(\theta_0 - \hat{\boldsymbol{\theta}}_0)(][\theta_0 - \hat{\boldsymbol{\theta}}_0)]^T \tag{14}$$

Step 2: Calculate the iterative form of the correction term ε_k.

$$\varepsilon_k = \boldsymbol{G}_k e_k \tag{15}$$

Step 3: Calculate the innovation value e_k of the system at each moment.

$$\boldsymbol{e}_k = y_k - \boldsymbol{\varphi}_k{}^T \hat{\boldsymbol{\theta}}_{k-1} \tag{16}$$

Step 4: Calculate the gain matrix $\boldsymbol{G}_k$.

$$\boldsymbol{G}_k = (\boldsymbol{P}_{k-1}\boldsymbol{\varphi}_k)/(\lambda + \boldsymbol{\varphi}_k{}^T \boldsymbol{P}_{k-1}\boldsymbol{\varphi}_k) \tag{17}$$

Step 5: Update the error covariance matrix P_k.

$$\boldsymbol{P}_k = (\boldsymbol{E} - \boldsymbol{G}_k \boldsymbol{\varphi}_k{}^T)\boldsymbol{P}_{k-1}/\lambda \tag{18}$$

Step 6: Update the system to be identified parameter matrix $\hat{\boldsymbol{\theta}}_k$.

$$\hat{\boldsymbol{\theta}}_k = \hat{\boldsymbol{\theta}}_{k-1} + \boldsymbol{G}_k (y_k - \boldsymbol{\varphi}_k{}^T \hat{\boldsymbol{\theta}}_{k-1}) \tag{19}$$

Step 7: Repeat steps 2 to 6 and iterates until the end of the entire world sequence.

In the calculation and update of the above iterative recursive process, $\boldsymbol{G}_k$ is the iterative gain matrix of the FFRLS algorithm. y_k represents the measured value of the terminal voltage of the system at time k and e_k is the new information of the system. λ is the forgetting factor, which is usually between 0.95 and 1, and the value in this paper is 0.98.

The FFRLS is used to identify the full parameters of the model at high frequencies and the

parameter of the small-time constant in the identification results is obtained. This parameter value can better characterize the internal charge transfer process and the electric double layer effect of the lithium-ion battery. Considering the influence of the battery's multi-time scale effect, this paper chooses the extended Kalman filter (EKF) as the model parameter identification algorithm under low frequency. When using the EKF algorithm to estimate model parameters, first the state space equation of the battery lumped electrical characteristic model is constructed as expressed in Equation (20).

$$\begin{cases} \rho_k = \rho_{k-1} + w_k \\ y_k = h(SOC_k, u_k, \rho_k) + v_k \end{cases} \tag{20}$$

In Equation (20), ρ_k is the parameter matrix at time k, and its matrix is characterized as: $\boldsymbol{\rho}_k = [R_{0,k} \quad R_{2,k} \quad C_{2,k}]^T$, y_k is the terminal voltage output vector at time k, u_k is the input current of the system at time k, $h(*,*,*)$ is the systematic observation equation, $\boldsymbol{w}_k$ is the modeling disturbance of the system and $\boldsymbol{v}_k$ is the observation noise of the system. Assuming that the errors of the system are all independent and identically distributed Gaussian white noises, the covariance matrix of $\boldsymbol{w}_k$ and $\boldsymbol{v}_k$ is obtained as shown in Equation (21).

$$\begin{cases} \sum_w = E(w \times w^T) \\ \sum_v = E(v \times v^T) \end{cases} \tag{21}$$

Using the open-circuit voltage, hysteresis voltage, and output voltage of the impedance circuit in the lumped electrical characteristic model given above, a specific form of the system observation equation is obtained, as shown in Equation (22).

$$h(SOC_k, u_k, \rho_k) = h(SOC_k, I_k, (R_{0,k}, R_{2,k}, C_{2,k})) = U_{OC}(SOC_k) + U_{h,k} - I_k R_{0,k} - U_{1,k} - U_{2,k} \tag{22}$$

The EKF algorithm is then applied to the online parameter identification of the battery lumped electrical characteristic model. The main iterative steps of the algorithm are as follows.

(1) Initialize the parameter matrix and the error covariance matrix.

$$\hat{\rho}_0 = E(\rho_0), \sum_0 = E[(\hat{\rho}_0 - \rho_0)(\hat{\rho}_0 - \rho_0)^T] \tag{23}$$

(2) Calculate the time update, as shown in Equation (24).

$$\begin{cases} \hat{\rho}_k^- = \hat{\rho}_{k-1} \\ \sum_k^- = \sum_{k-1} + \sum_w \end{cases} \tag{24}$$

(3) Calculate the measurement update, as shown in Equation (25).

$$\begin{cases} K_k^\rho = \sum_k^- (\boldsymbol{C}_k^\rho)^T [\boldsymbol{C}_k^\rho \sum_k^- (\boldsymbol{C}_k^\rho)^T + \sum_v]^{-1} \\ \hat{\rho}_k = \hat{\rho}_k^- + K_k^\rho [y_k - h(x_k, u_k, \hat{\rho}_k^-)] \\ \sum_k = (I - K_k \boldsymbol{C}_k^\rho) \sum_k^- \end{cases} \tag{25}$$

According to Equation (24) and Equation (25), $\hat{\rho}_k^-$ is the prior parameter estimate. $\hat{\rho}_k$ is posterior parameter estimate, $\sum_k$ is the error covariance matrix, and K_k^ρ is the gain matrix. When the EKF algorithm is used to identify the parameters of the model, the linearized observation matrix is obtained by locating the partial derivative of the observation equation. The calculation of the observation matrix is shown in Equation (26).

$$\boldsymbol{C}_k^\rho = \left. \frac{\partial h(SOC_k, u_k, \rho)}{\partial \rho} \right|_{\rho = \hat{\rho}_k^-} = \left[\frac{\partial h(SOC_k, u_k, \hat{\rho}_k^-)}{\partial R_{0,k}}, \frac{\partial h(SOC_k, u_k, \hat{\rho}_k^-)}{\partial R_{2,k}}, \frac{\partial h(SOC_k, u_k, \hat{\rho}_k^-)}{\partial C_{2,k}} \right] \tag{26}$$

The parameter identification iteration based on EKF includes time and measurement updates. The measurement update completes the iterative calculation of the algorithm, and the time update obtains the optimal parameter matrix to be identified in the iterative process. It should be emphasized that when using FFRLS and EKF algorithms to collaboratively identify model parameters, the starting conditions for asynchronous identification need to be given. Since the driving conditions of electric vehicles are accompanied by strong uncertainty, this paper takes the change of SOC as the judgment condition for the large-time constant identification. The amount of SOC change and the calculation method of SOC at each time is shown in Equation (27).

$$\begin{cases} \Delta SOC = (\int \eta I dt) \big/ Q_N = \eta I \Delta t / Q_N \\ SOC_{k+1} = SOC_k - \eta I \Delta t / Q_N \end{cases} \tag{27}$$

In Equation (27), Q_N represents the rated battery capacity and η is the Coulomb efficiency. Due to the limited experimental conditions, this paper does not consider the related experiments of Coulomb correction and therefore, takes η as 1. The working condition current of the car not only changes in magnitude but also changes in direction. Compared with the judgment condition of fixed large step size, the judgment method of Equation (27) can make the asynchronous identification algorithm adapt to a variety of current working conditions, enhance the identification precision of the system and reduce the calculation complexity of the system. In addition, this paper uses root-mean-square error (RMSE), mean absolute percentage error (MAPE), and maximum error (MAXE) to describe the estimation performance of the model, and the calculation method is shown in Equation (28).

$$RMSE = \sqrt{\frac{1}{n}\sum_{i=1}^{n}\left(y_i - \hat{y}_i\right)^2}, \quad MAPE = \frac{1}{n}\sum_{i=1}^{n}\frac{\left|y_i - \hat{y}_i\right|}{y_i} \times 100\%, \quad MAXE = Max\left|y_i - \hat{y}_i\right| \tag{28}$$

where y_i is the observed value of the terminal voltage, $\hat{y}_i$ is the estimated value of terminal voltage, and n is the total number of samples.

2.4.2 Algorithm for adaptive full-parameter identification

Through the core idea of asynchronous parameter identification, the adaptive parameter identification of the LEC is realized, which greatly improves the management efficiency of vehicle-mounted BMS. According to the identification framework of the AAPIS, a simplified code suitable for system online applications is given, as shown in Table 1.

Table 1. Adaptive multi-time scale online parameter identification simplified code

1	**Procedure: Model full parameter identification**
2.	**for** k = 0 to 2

3. Give the initialization matrix: $\widehat{\boldsymbol{\theta}}_k, \hat{\rho}_k, P_k, Q_k, R_k, U_2$

4. **end for**

5. **while** $k > N$

6. **for** k=3 to N

7. Calculate the innovation value of the system at each moment: Equation (16)

8. Calculate the gain matrix of the iterative algorithm G_k: Equation (17)

9. Update the error covariance matrix of the iterative algorithm P_k: Equation (18)

10. Update the system parameter matrix to be identified $\widehat{\boldsymbol{\theta}}_k$: Equation (19)

11. Output model parameters: R_0, R_1, C_1

12. **while** $\Delta SOC \geq 0.5\%$

13. Use EKF algorithm to identify model parameters at low frequencies

14. Time update in EKF algorithm: Equation (24)

15. Measurement update in EKF algorithm: Equation (25)

16. Output model parameters: R_0, R_2, C_2

17. Update the value of U_2 in the FFRLS algorithm

18. **end while**

19. Output R_0 value after the arithmetic average

20. **end for**

21. **end while**

22. **end procedure**

In Table 1, the size of ΔSOC is the judgment condition for whether the EKF algorithm is started or not. The capacity value Q_N involved in the calculation method can be obtained through capacity calibration experiments. The adaptive multi-time scale online parameter identification strategy is revised

and updated in the iterative process, to complete the model parameter identification and update of the entire time series.

3 Experiments and results analysis

3.1 Battery sample and experimental platform

To verify the accuracy of the model and the estimated effect of the AAPIS algorithm on the actual working conditions, an experimental platform is built as shown in Figure 3(a). The entire experimental platform includes a battery test system, a temperature test chamber, and a host computer. Among them, the functions of the battery test system are to simulate the actual driving conditions of electric vehicles, the temperature test chamber is used to provide a constant temperature for the battery sample, and the host computer is used to collect relevant experimental data, including temperature, current and voltage, and complete signal feedback. Secondly, a battery sample is selected and this article selects a ternary lithium-ion battery with a rated capacity of 50Ah as the experimental sample. The detailed information on the battery sample is shown in Figure 3(b). In addition, it should be noted that in this work, the full parameter identification of the battery lumped electrical characteristic model and the verification of AAPIS are completed at 25°C, and the experimental analysis at multiple temperatures is carried out in the next step.

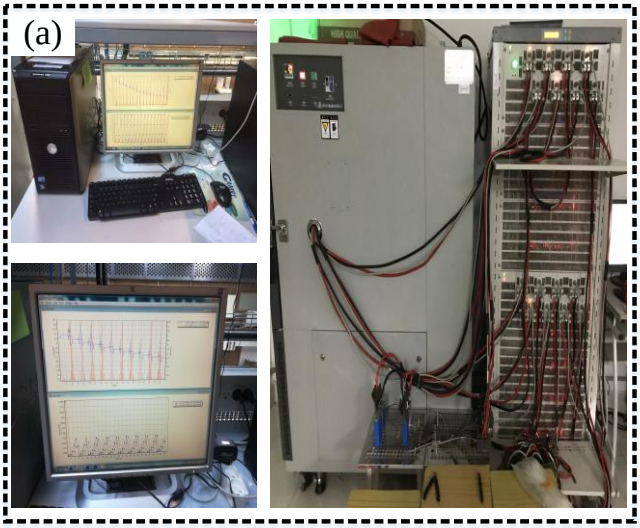

Fig. 3 Experimental platform and battery sample parameters

3.2 Multi-time scale identification results under CCDPT

To precision identify the full parameters of the lumped electrical characteristic model under AAPIS, a complex charge-discharge pulse test (CCDPT) is designed in this article. The CCPDPT takes into account the uncertainty and complexity of the use conditions of electric vehicles and adopts a variety of combinations of different magnifications to perform mixed charge and discharge tests on battery samples, which greatly restores the actual operating conditions of electric vehicles. In addition, due to the hysteresis characteristics of the open-circuit voltage, the high-accuracy OCV-SOC characterization equation needs to consider the hysteresis characteristics and OCV of the battery. In the OCV acquisition phase, this work uses the SOC interval of 0.02 to conduct a discharge-shelving experiment, and obtain discharge OCV values at different SOC. Then, the constant current charging experiment was carried out with the same experimental procedure, and the charging OCV values under different SOC were also obtained. The OCV value under different charging and discharging conditions lay a data foundation for the calibration of the OCV-SOC function and the calculation of $M(SOC_k)$.

Two sets of tests are performed on the battery samples using the above test methods. The two sets of discharge-shelving experiment results obtained are mathematically averaged to improve the

measurement precision of the OCV of the battery sample. The current and terminal voltage curve of the CCDPT process, the OCV-SOC calibration test curve, and the relevant data curve of $M(SOC_k)$ are shown in Fig. 4.

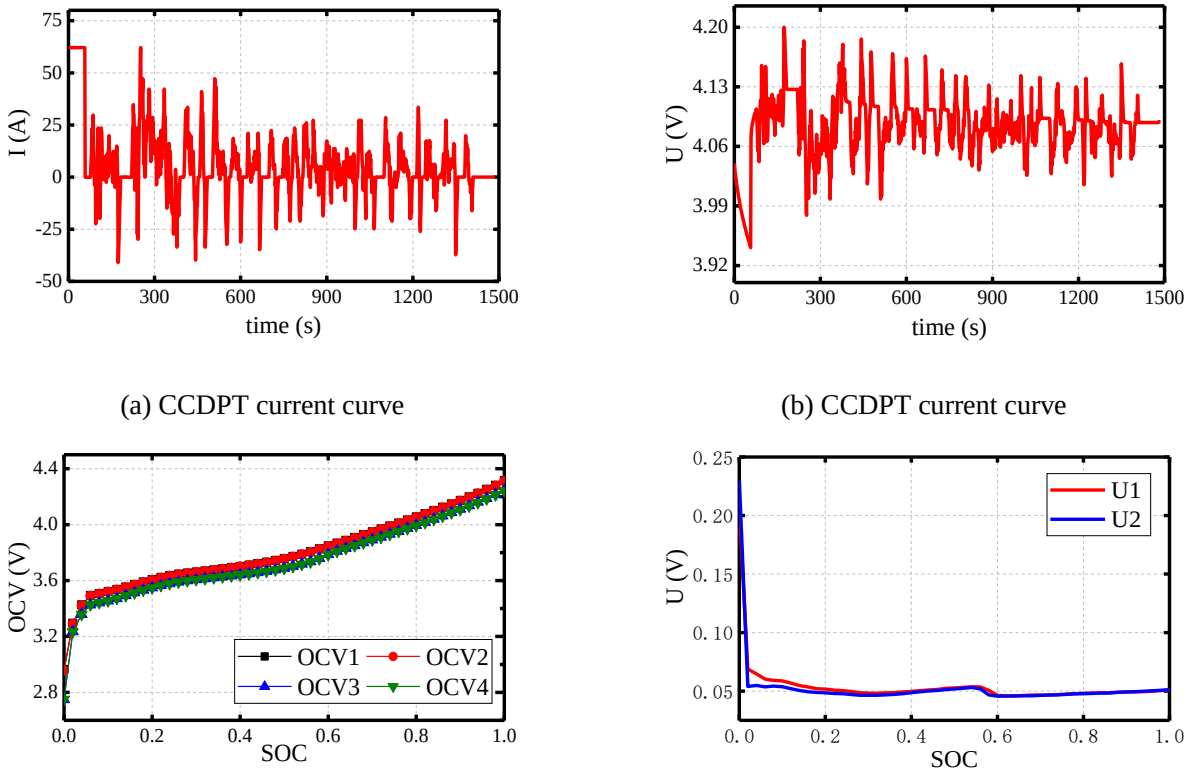

(a) CCDPT current curve

(b) CCDPT current curve

(c) OCV-SOC curve

(d) $M(SOC_k)$ curve

Fig. 4 CCDPT results and OCV-SOC calibration curve

Fig. 4(a) and (b) are the current process curve and terminal voltage process curve of CCPDPT respectively. Fig. 4(c) shows two sets of OCV calibration experimental curves, in which OCV1 and OCV2 are OCV measurement values in the charging state, and OCV3 and OCV4 are OCV measurement values in the discharging state. Fig. 4(d) is the calculation result curve of the two sets of $M(SOC_k)$, which is used to calculate the value of the hysteresis voltage U_h. Among them, U1 is the hysteresis voltage value in the charging state, and U2 is the hysteresis voltage value in the discharging state. In addition, it can be seen from Fig. 4(c) that the OCV values in the same state (the same discharging state or the same

charging state) are almost the same, and the OCV values under different states are quite different, and the OCV value in the charging state is larger than the OCV value in the discharging state.

The OCV-SOC function of the battery needs to be calibrated before model parameter identification. First, the above two groups of OCV-SOC calibration experimental data under the same state are mathematically averaged. Secondly, SOC is taken as the independent variable, the OCV value at the corresponding time as the dependent variable, and formula 1 as the objective function. Finally, through function custom fitting, the OCV-SOC function of the selected battery sample is obtained. The results are shown in Table 2.

Table 2 OCV-SOC function calibration results

General model (Charge state): $U_{OC}(SOC_k) = f(SOC_k) = m_1 + m_2 \ln(SOC_k) + m_3 \ln[1-(SOC_k)]$ **Coefficients (with 95% confidence bounds):** m_1=3.759 (3.725, 3.792) m_2=0.1164 (0.09852, 0.01343) m_3=-0.1685 (-0.1863, -0.1506)	**Goodness of fit:** SSE:0.06443 R-square:0.9764 Adjusted R-square:0.9754 RMSE:0.03743
General model (discharge state): $U_{OC}(SOC_k) = f(SOC_k) = m_1 + m_2 \ln(SOC_k) + m_3 \ln[1-(SOC_k)]$ **Coefficients (with 95% confidence bounds):** m_1=3.701 (3.666, 3.736) m_2=0.1179 (0.09939, 0.1364) m_3=-0.1667(-0.1852, -0.1481)	**Goodness of fit:** SSE:0.06904 R-square:0.9747 Adjusted R-square:0.9736 RMSE:0.03874

It can be seen from Table 2 that the root mean square error of the curve fitting of the OCV-SOC function after mathematical averaging is small and the precision is high. Through the system's judgment

of the positive and negative current, the present state of the battery is obtained, and then different OCV-SOC functions are used to identify the parameters of the battery. The CCPDPT process data is used to program the algorithm with Table 1 as the framework to realize the full parameter identification of the model. The result is shown in Fig. 5.

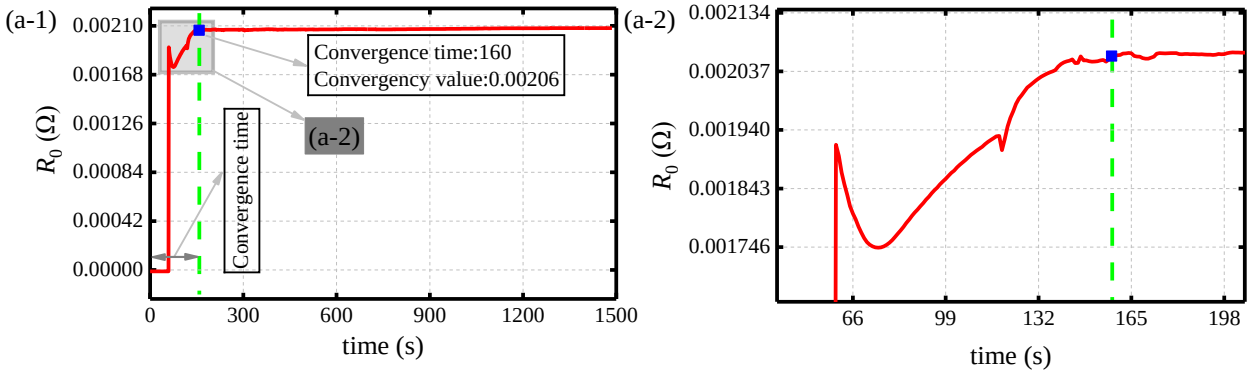

(a) Convergence time and identification result of R_0

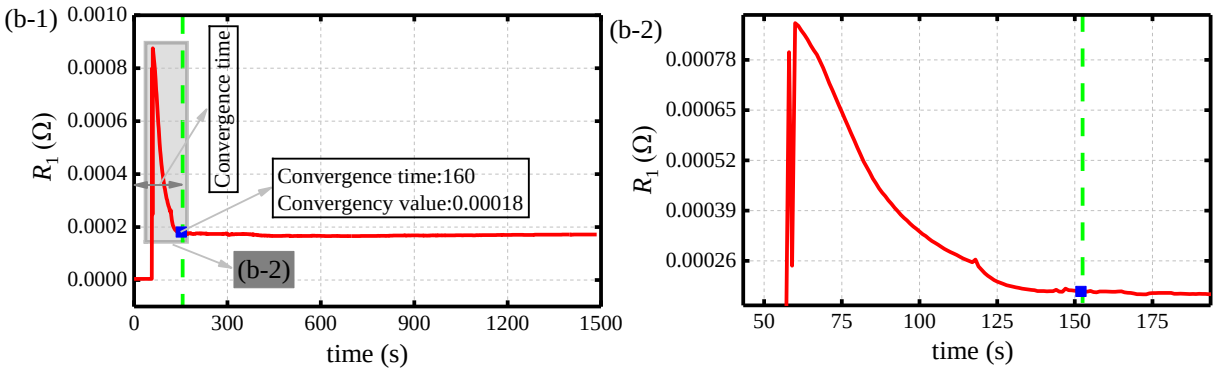

(b) Convergence time and identification result of R_1

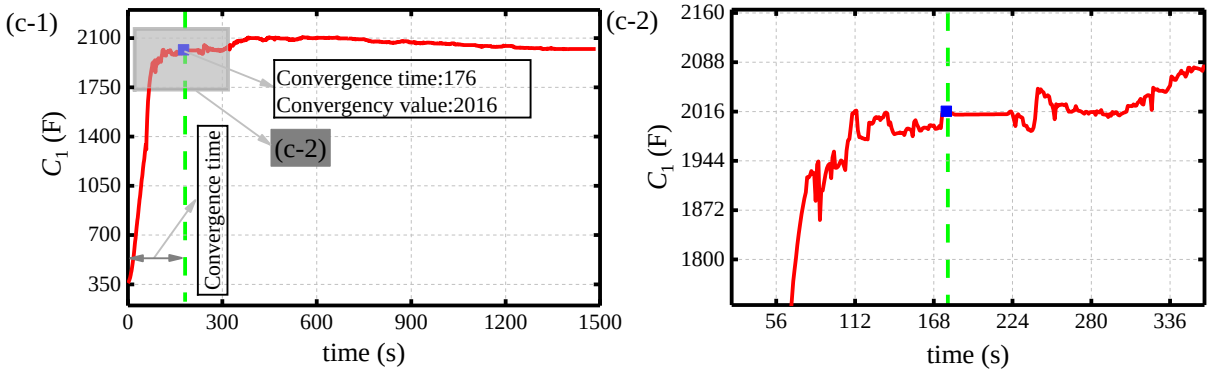

(c) Convergence time and identification result of C_1

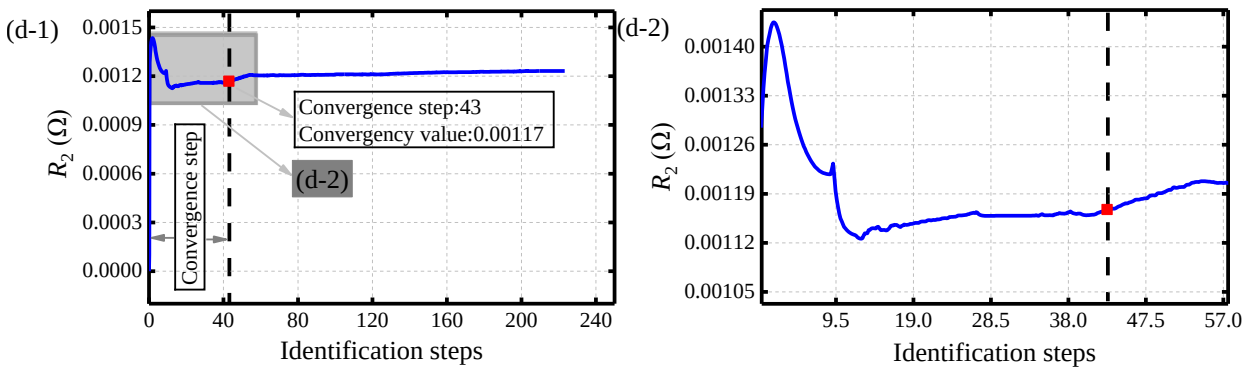

(d) Convergence time and identification result of R_2

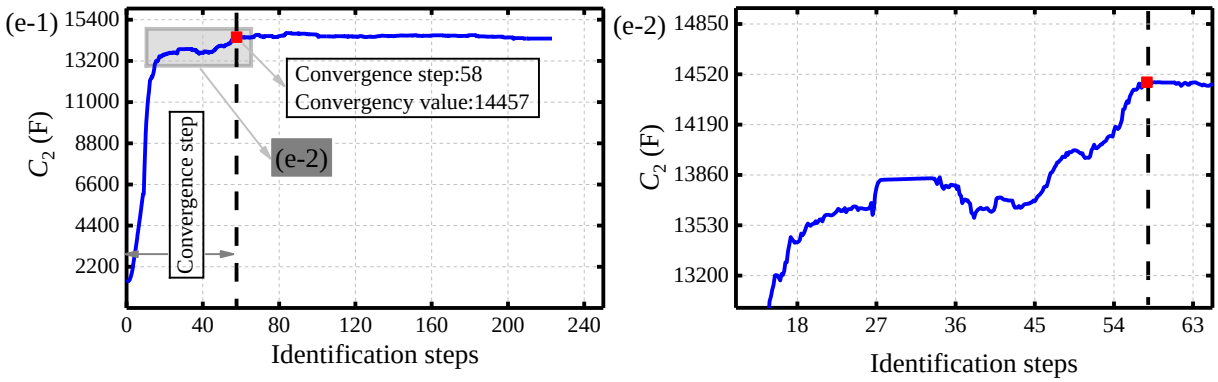

(e) Convergence time and identification result of C_2

Fig. 5 The full parameter identification result of LECM

Due to the multi-time scale effect of the battery, it is difficult for the parameter identification result under a single time scale to simultaneously characterize the internal mechanism of the battery. According to the idea of adaptive asynchronous parameter identification, the identification steps of R_0, R_1 and C_1 are relatively short, and the system sampling time is used as a fixed step for identification, as shown in Fig. 5(a-c). The identification of R_2 and C_2 uses the change of SOC as the adaptive step size for identification, as shown in Fig. 5(d-e). From the above identification results, it can be seen that the convergence of each parameter is different. Among them, the convergence of R_0, R_1 and C_1 is characterized by convergence time, and the convergence of R_2 and C_2 is characterized by convergence steps. In addition, it can be seen from the convergence value of each parameter of the model that the time constant corresponding to the R_1C_1 link is smaller, and the time constant corresponding to the R_2C_2 link is larger. It shows that AAPIS can simultaneously characterize the electric double layer effect of the

internal charge of the battery and the diffusion effect of ions in the solid particles.

3.3 AAPIS validation under CCDPT and MDPT

The parameter identification results of the model can only be used to illustrate the rationality of the algorithm in characterizing the internal effects of the battery. The judgment of the model accuracy depends on the estimation precision of the battery terminal voltage. In this work, the identification precision of FFRLS under a single-time scale is compared with that of AAPIS under a multi-time scale, and the terminal voltage error curves under two identification strategies are given, and the results are shown in Fig. 6.

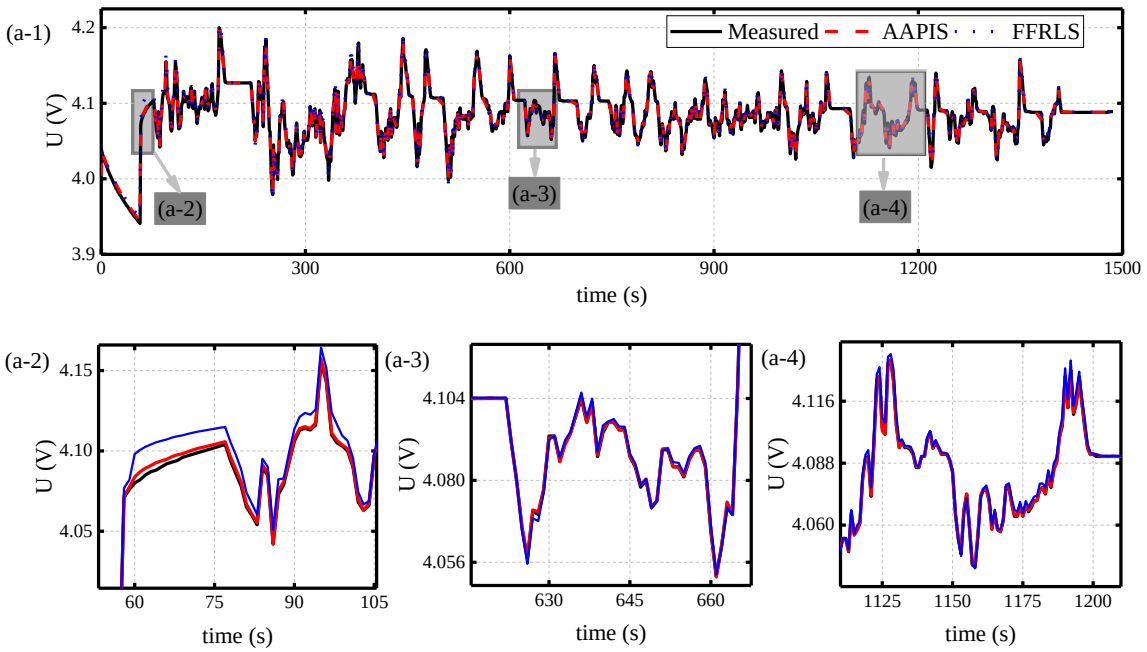

(a) Comparison result of terminal voltage under CCDPT

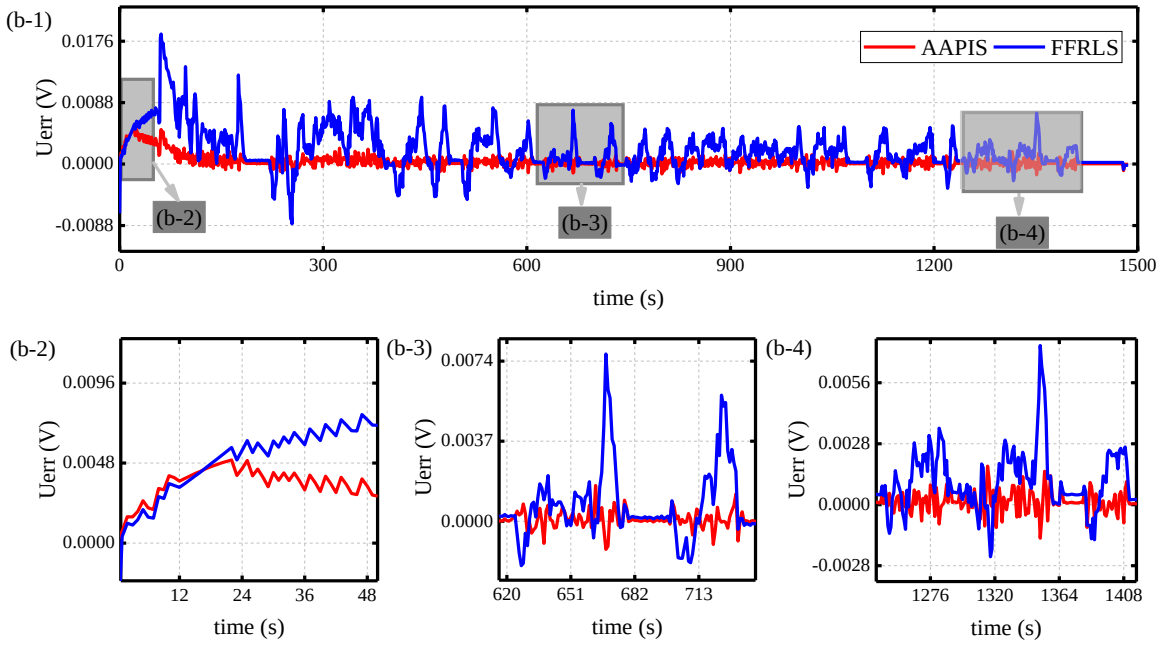

(b) Comparison result of terminal voltage error under CCDPT

Fig.6 Comparison of terminal voltage error curves under CCDPT

Fig. 6(a) is a comparison curve of the estimated value and the true value of the terminal voltage obtained by using different identification strategies under CCDPT. Fig. 6(b) shows the error comparison curve between the estimated value and the true value of the terminal voltage under different identification strategies. It can be seen from Fig. 6 that under the CCDPT working condition, the maximum estimation error of the terminal voltage of the multi-time scale AAPIS is 4.98 mV, and the accuracy is 0.011%. The maximum estimation error of the terminal voltage of FFRLS under a single time scale is 18.63 mV, and the precision is 0.43%. In comparison, the precision of the multi-time scale AAPIS is increased by 0.42%. In addition, according to Fig. 6(b), it can be seen that the convergence time of the multi-time scale AAPIS is 24 s, and the overall estimation error fluctuation is small. The convergence time of FFRLS under a single time scale is 280 s, and the overall estimation error fluctuates greatly. It can be concluded that the AAPIS has higher accuracy and stronger robustness.

CCDPT operating conditions can explain the high accuracy of AAPIS to a certain extent. However, due to the short duration of CCDPT, the diffusion effect inside the battery cannot be intuitively reflected.

To further verify the accuracy of LECM and the superiority of AAPIS, this paper designs a mixed discharge pulse test (MDPT). In this experiment, the battery samples were discharged for 20 s, left for 45 s, charged for 20 s, left for 45 s, and discharged for 330 s. Among them, the short-term charge and discharge of 20 s are used to verify the electric double layer effect of the battery, and the long-term discharge of 330 s is used to verify the diffusion effect of the battery. Similarly, based on the MDPT experiment, the identification precision of the FFRLS under a single-time scale is compared with the identification precision of AAPIS under a multi-time scale and the terminal voltage error curves under the two identification strategies are given. The results are shown in Fig. 7.

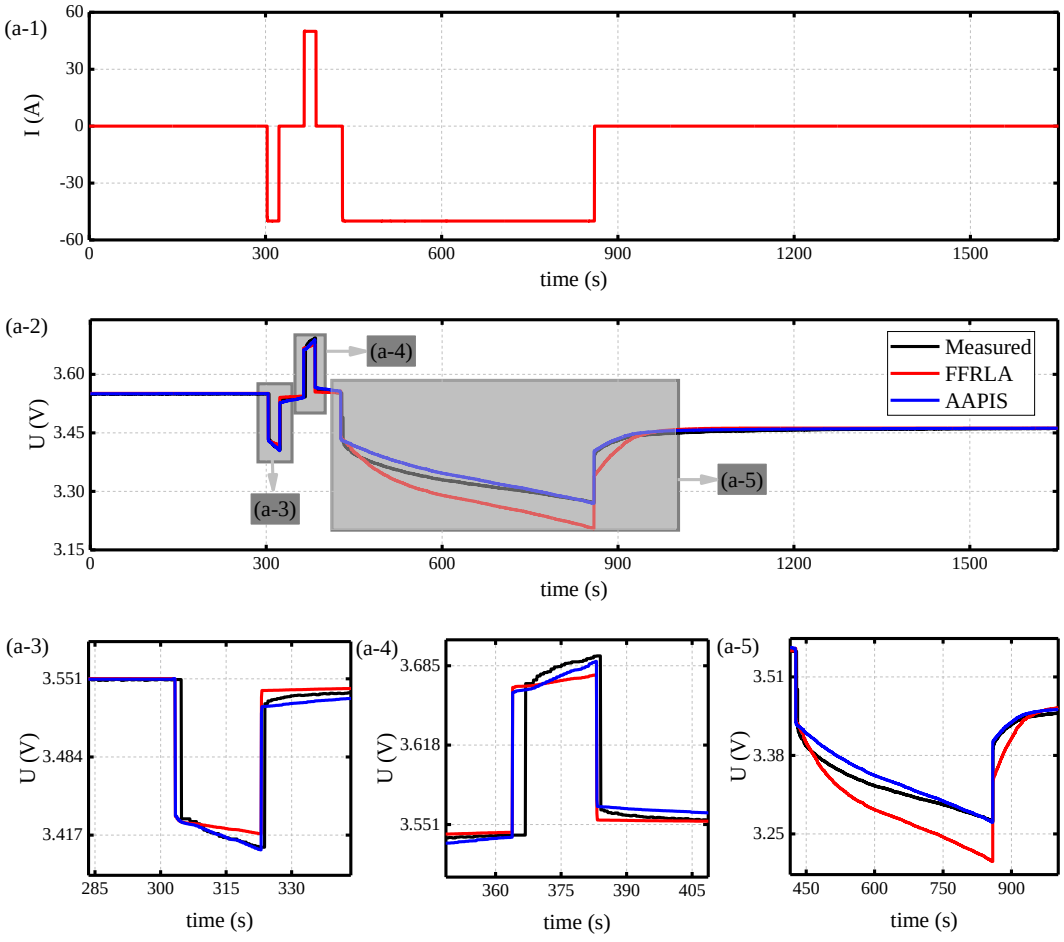

(a) Comparison result of terminal voltage under MDPT

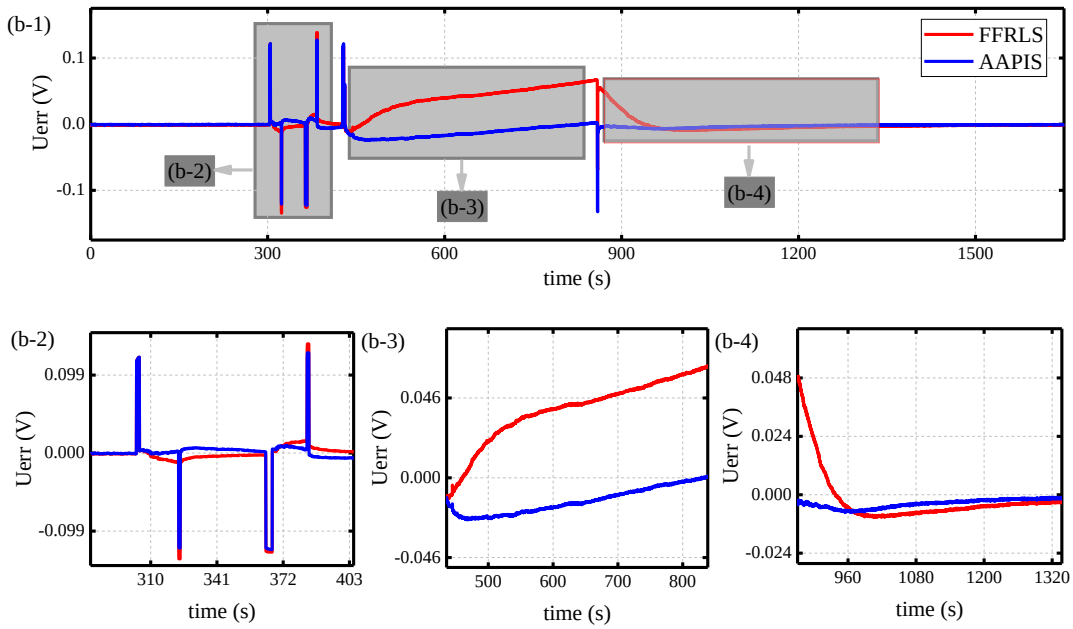

(b) Comparison result of terminal voltage error under MDPT

Fig. 7 Comparison of terminal voltage error curves under MDPT

Fig. 7(a-1) describes the MDPT current curve, Fig. 7(a-2) describes the MDPT terminal voltage comparison curve under different identification strategies, Fig. 7(a-3), (a-4), and (a-5) depict the partial magnification curves of charge and discharge pulses in MDPT, Fig. 7(b-1) describes the MDPT terminal voltage error comparison curve under different identification strategies and Fig. 7(b-2), (b-3), and (b-4) are the partial amplification curves of the terminal voltage error.

It can be seen from Fig. 7(a-3), (a-4), and (a-5) that the AAPIS has a very strong terminal voltage tracking capability in both the long-term discharge and the short-term pulse discharge stages. Fig. 7(b-2) shows that the short-time pulse charge and discharge phase cannot trigger the judgment condition of $\Delta SOC \geq 0.5\%$ in AAPIS, which makes the single-time-scale FFRLS and multi-time-scale AAPIS have large errors. The maximum errors of the two identification strategies are 139.12 mV and 122.38 mV respectively. Fig. 7(b-3) shows that with the progress of the long-term discharge process, the accumulation of current enables the judgment condition of $\Delta SOC \geq 0.5\%$ to be satisfied, which in turn enables the superiority of the multi-time scale AAPIS to be demonstrated. The maximum errors of the

two identification strategies at this stage are 68.59 mV and 21.80 mV, respectively. Fig. 7(b-4) shows that the terminal voltages obtained by the two identification strategies have been converged, but the multi-time-scale AAPIS still has higher accuracy than the single-time-scale FFRLS. The maximum errors of the two identification strategies after convergence are 9.34 mV and 7.42 mV, respectively, and the convergence speed of multi-time scale AAPIS is higher than that of single-time-scale FFRLS. The above experiment fully verified the feasibility and superiority of the online adaptive asynchronous parameter identification strategy of the lumped parameter electrical characteristic model.

To visually show the performance pros and cons of different algorithms, this paper uses three different indicators of RMSE, MAPE, and MAXE to quantitatively analyze the accuracy of modeling. The terminal voltage tracking effects under the single-time-scale FFRLS algorithm and the multi-time-scale AAPIS algorithm are listed, as shown in Table 3. It should be noted that, compared to CCDPT operating conditions, MDPT operating conditions are single-pulse operating conditions, and fewer current pulses make the advantages of modeling the hysteresis characteristics of open-circuit voltage not fully highlighted. Therefore, the values of RMSE, MAPE, and MAXE under MDPT conditions are relatively large. The identification accuracy under CCDPT conditions is higher than that of reference [33] (the RMSE value of the terminal voltage under complex discharge rate is 8.7 mV), which is 7.72 mV higher than that of reference [41] (the terminal voltage MAXE value under the complex discharge rate is 11 mV) increase 5.02 mV. It can verify the superiority of the online adaptive asynchronous parameter identification strategy based on the lumped parameter electrical characteristic model.

Table 3 Comparison of RMSE, MAPE, and MAXE errors under CCDPT and MDPT conditions

Experimental conditions	CCDPT			MDPT		
Evaluation index	RMSE (mV)	MAPE (%)	MAXE (mV)	RMSE (mV)	MAPE (%)	MAXE (mV)

FFRLS	3.60	0.06	18.63	80.01	4.37%	139.12
AAPIS	0.98	0.01	4.98	38.48	1.68%	122.38

3.4 Parameter consistency verification analysis

In addition to measuring the quality of the model and the identification strategy by the terminal voltage, it is also necessary to consider the physical meaning of the internal parameters of the model. The direct manifestation of the unclear physical meaning is that the parameter identification results are different under different working conditions. Therefore, the analysis of parameter consistency under different identification strategies is particularly important. Based on LECM, this paper normalizes the identification results under FFRLS and AAPIS to achieve the consistency check of the parameter identification results. The results are shown in Fig. 8.

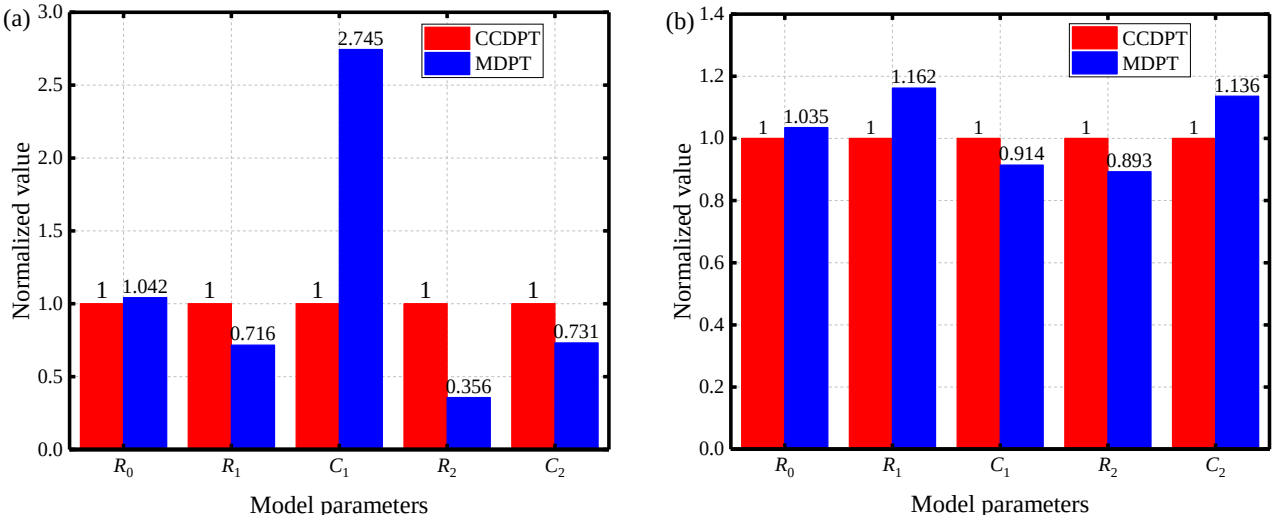

(a) Consistency results under single-time-scale FFRLS (b) Consistent results under multi-time-scale AAPIS

Fig. 8 Normalized results of parameters under FFRLS and AAPIS

Fig. 8(a) shows the normalized results of parameters under two working conditions in single-time-scale FFRLS. Fig. 8(b) shows the normalized results of the parameters under the two working conditions in the multi-time-scale AAPIS. It can be seen from Fig. 8(a) that the maximum error of parameter consistency of FFRLS without constraints under different working conditions is 174.5%. It shows that

its physical meaning is not obvious, and using this result to estimate other states of the battery will produce larger errors. At the beginning of the design of the multi-time scale AAPIS, the internal physical meaning of the parameters was considered. Therefore, it can be seen from Fig. 8(b) that the maximum consistency error of the parameter identification result based on AAPIS is 16.2%, and this result can be used to estimate other states of the battery.

4 Conclusion

In this work, the starting point is to solve the influence of the battery's multi-time scale effect on the online parameter identification algorithm, aiming to realize the optimal online identification of the battery's internal parameters. By considering and realizing the inherent hysteresis characteristic modeling of the battery open-circuit voltage, a lumped electric characteristic model of the vehicle-mounted lithium-ion battery with a wide range of applications is established. Then, the frame design of an adaptive asynchronous parameter identification strategy is designed to enhance the precision of the system identification. In addition, based on the lumped electrical characteristic model and the adaptive asynchronous parameter identification strategy, the process design of the simplified code for online parameter identification is completed. Finally, the CCDPT and MDPT working conditions are designed, and the identification result and terminal voltage tracking effects under single-time-scale FFRLS and multi-time-scale AAPIS are compared and analyzed. The results fully verify the feasibility and superiority of AAPIS. In addition, given the physical meaning of the internal parameter identification result of the model, the identification results under different identification methods are normalized. The results show that the consistency of the parameter identification result of AAPIS under different working conditions is higher, and the parameter consistency is the largest, and the error value is reduced by 158.3%. It fully illustrates that the parameter identification results under AAPIS can provide a data basis

for subsequent estimation of other battery states.

Acknowledgments

This research was supported by National Natural Science Foundation (No. 61801407). Thanks to the sponsors. CF would like to express his gratitude to RGU for its support.

References

[1] Wang, Y.J.; Chen, Z.H. A framework for state-of-charge and remaining discharge time prediction using unscented particle filter. *Applied Energy* **2020**, *260*, 114324.

[2] Khalik, Z.; Donkers, M.; Bergveld, H.J. Model simplifications and their impact on computational complexity for an electrochemistry-based battery modeling toolbox. *Journal of Power Sources* **2021**, *488*, 229427.

[3] Ouyang, M.G.; Du, J.Y.; Peng, H.E.; Wang, H.W.; Feng, X.N.; Song, Z.Y. Progress review of US-China joint research on advanced technologies for plug-in electric vehicles, *Sci China Technol Sc* **2018**, *61*, 1431-1445.

[4] Pramanik, S.; Anwar, S.; Electrochemical model-based charge optimization for lithium-ion batteries. *Journal of Power Sources* **2016**, *313*, 164-177.

[5] Zhang, K., Zhao, P., Sun, C.F., Wang, Y.R., Chen, Z.W. Remaining useful life prediction of aircraft lithium-ion batteries based on F-distribution particle filter and kernel smoothing algorithm. *Chinese Journal of Aeronautics* **2020**, *33*, 1517-1531.

[6] Xu, Y.D.W., Xu, J.L., Yan, X.F. Lithium-ion battery state of charge and parameters joint estimation using cubature Kalman filter and particle filter. *Journal of Power Electronics* **2020**, *20*, 292-307.

[7] Lee, K.T.; Dai, M.J.; Chuang, C.C.; Temperature-Compensated Model for Lithium-Ion Polymer Batteries with Extended Kalman Filter State-of-Charge Estimation for an Implantable Charger, *IEEE Transactions on Industrial Electronics* **2018**, *65*, 589-596.

[8] Tian, J.P.; Xiong, R.; Yu, Q.Q. Fractional-Order Model-Based Incremental Capacity Analysis for Degradation State Recognition of Lithium-Ion Batteries, *IEEE Transactions on Industrial Electronics* **2019**, *66*, 1576-1584.

[9] Voskuilen, T.G., Moffat, H.K., Schroeder, B.B., Roberts, S.A. Multi-fidelity electrochemical modeling of thermally activated battery cells. *Journal of Power Sources* **2021**, *488*, 229469.

[10] Shen, P.; Ouyang, M.G.; Lu, L.G.; Li, J.Q.; Feng, X.N. The Co-estimation of State of Charge, State of Health, and State of Function for Lithium-Ion Batteries in Electric Vehicles, *IEEE T Veh Technol* **2018**, *67*, 92-103.

[11] Guo, F.; Hu, G.D.; Zhou, P.K.; Hu, J.Y.; Sai, Y.H. State of charge estimation in electric vehicles at various ambient temperatures. *International Journal of Energy Research* **2020**, *44*, 7357-7370.

[12] Wang, Q.T.; Qi, W. New SOC estimation method under multi-temperature conditions based on parametric-estimation OCV. *Journal of Power Electronics* **2020**, 20, 614-623.

[13] Afshari, H.H.; Attari, M.; Ahmed, R.; Delbari, A.; Habibi, S.; Shoa, T. Reliable state of charge and state of health estimation using the smooth variable structure filter, *Control Eng Pract* **2018**, *77*, 1-14.

[14] Wang, S.L.; Fernandez, C.; Chen, M.J.; Wang, L.; Su, J. A novel safety anticipation estimation method for the aerial lithium-ion battery pack based on the real-time detection and filtering, *J Clean Prod* **2018**, *185*, 187-197.

[15] Zhang, Z.L.; Cheng, X.; Lu, Z.Y.; Gu, D.J. SOC Estimation of Lithium-Ion Battery Pack Considering Balancing Current, *Ieee T Power Electr* **2018**, 33, 2216-2226.

[16] Wang, W.D.; Wang, X.T.; Xiang, C.L.; Wei, C.; Zhao, Y.L. Unscented Kalman Filter-Based Battery SOC Estimation and Peak Power Prediction Method for Power Distribution of Hybrid Electric Vehicles, *IEEE Access* **2018**, *6*, 35957-35965.

[17] Zhang, Y.; Peng, Z.; Guan, Y. Prognostics of battery cycle life in the early-cycle stage based on hybrid model. *Energy* **2021**, *221*.

[18] Fenner, G.P.; Stringini, L.W.; Rangel, C. Comprehensive Model for Real Battery Simulation Responsive to Variable Load. *Energies* **2021**, *14*.

[19] Bruen, T.; Marco, J. Modelling and experimental evaluation of parallel connected lithium-ion cells for an electric vehicle battery system. *Journal of Power Sources* **2016**, *310*, 91-101.

[20] Bruch, M.; Millet, L.; Kowal, J. Novel method for the parameterization of a reliable equivalent circuit model for the precise simulation of a battery cell's electric behavior. *Journal of Power Sources* **2021**, *490*, 229513.

[21] Feng, X.N.; Weng, C.H.; Ouyang, M.G. Online internal short circuit detection for a large format lithium-ion battery. *Applied Energy* **2016**, *161*, 168-180.

[22] Fridholm, B.; Wik, T.; Nilsson, M. Robust recursive impedance estimation for automotive lithium-ion batteries. *Journal of Power Sources* **2016**, *304*, 33-41.

[23] Barai, A.; Uddin, K.; Widanage, W.D.; McGordon, A.; Jennings, P. A study of the influence of measurement timescale on internal resistance characterisation methodologies for lithium-ion cells, *Sci Rep* **2018**, *8*.

[24] Xu, C.; Cleary, T.; Wang, D. Online state estimation for a physics-based Lithium-Sulfur battery model. *Journal of Power Sources* **2021**, *489*, 229495.

[25] Ragone, M.; Yurkiv, V.; Ramasubramanian, A. Data driven estimation of electric vehicle battery state-of-charge informed by automotive simulations and multi-physics modeling. *Journal of Power Sources* **2021**, *483*, 229108.

[26] Mesbahi, T.; Rizoug, N.; Bartholomeus, P. Dynamic model of li-ion batteries incorporating electrothermal and ageing aspects for electric vehicle applications. *IEEE Transactions on Industrial Electronics* **2018**, *65*, 1298-1305.

[27] Wu, L.X.; Liu, K.; Pang, H. Evaluation and observability analysis of an improved re duce d-order electrochemical model for lithium-ion battery. *Electrochemica Acta* **2021**, *368*, 137604.

[28] Rahman, M.A.; Anwar, S.; Izadian, A. Electrochemical model parameter identification of a lithium-ion battery using particle swarm optimization method. *Journal of Power Sources* **2016**, *307*, 86-97.

[29] Wu, L.X.; Liu, K.; Pang, H. Online SOC Estimation Based on Simplified Electrochemical Model for Lithium-Ion Batteries Considering Current Bias. *energies* **2021**, *14*, 5265.

[30] Chen, L.; Wang, H.; Liu, B. Battery state-of-health estimation based on a metabolic extreme learning machine combining degradation state model and error compensation. *Energy* **2021**, *215*.

[31] Zhao, X.; Callafon, R.A. Modeling of battery dynamics and hysteresis for power delivery prediction and SOC estimation. *Applied Energy* **2016**, *180*, 823-833.

[32] Zou, Y.; Li, S.B.E.; Shao, B. State-space model with non-integer order derivatives for lithium-ion battery. *Applied Energy* **2016**, *161*, 330-336.

[33] Dai, H.F.; Xu, T.J.; Zhu, L.T. Adaptive model parameter identification for large capacity Li-ion batteries on separated time scales. *Applied Energy* **2016**, *181*, 119-131.

[34] Wang, S., Kuang, K., Han, X., Chu, Z., Ouyang, M.G. A model-based continuous differentiable current charging approach for electric vehicles in direct current microgrids. *Journal of Power Sources* **2021**, *482*, 229019.

[35] Hashemi, S.R.; Mahajan, A.M.; Farhad, S. Online Estimation of Battery Model Parameters and State of Health in Electric and Hybrid Aircraft Application. *Energy*, **2021**, *229*, 120699.

[36] Wang, M.L.; Li, H.X. Spatiotemporal modeling of internal states distribution for lithium-ion battery. *Journal of Power Sources* **2016**, *301*, 261-270.

[37] Wijewardana, S.; Vepa, R.; Shaheed, M.H. Dynamic battery cell model and state of charge estimation. *Journal of Power Sources* **2016**, *308*, 109-120.

[38] Jin, C.; Sun, Y.; Wang, H. Model and experiments to investigate thermal runaway characterization of lithium-ion batteries induced by external heating method. *Journal of Power Sources* **2021**, *504*, 230065.

[39] Yang, J.F.; Xia, B.; Shang, Y.L. Adaptive state-of-charge estimation based on a split battery model for electric vehicle applications. *IEEE Transactions on Vehicular Technology* **2017**, *66*, 10889-10898.

[40] Bruen, T.; Marco, J. Modelling and experimental evaluation of parallel connected lithium-ion cells for an electric vehicle battery system. *Journal of Power Sources* **2016**, *310*, 91-101.

[41] Shi H.T.; Wang, S.L.; Fernandez, C.; Yu C.M.; Fan Y.C.; Cao W. Improved splice-electrochemical circuit polarization modeling and optimized dynamic functional multi-innovation least square parameter identification for lithium-ion batteries, *International Journal of Energy Research* **2021**, *5*, 1-15.